Journal of Petroleum Science and Engineering 201 (2021) 108381

Contents lists available at ScienceDirect

Journal of Petroleum Science and Engineering

journal homepage: http://www.elsevier.com/locate/petrol

Stability and conductivity of proppant packs during flowback in unconventional reservoirs: A CFD–DEM simulation study

Federico G. Vega [a], C. Manuel Carlevaro [a,b,*], Martín Sánchez [c], Luis A. Pugnaloni [d]

[a] Instituto de Física de Líquidos y Sistemas Biológicos. CONICET La Plata - UNLP, Argentina, Calle 59 Número 789, La Plata, 1900, Buenos Aires, Argentina
[b] Universidad Tecnológica Nacional - Facultad Regional La Plata, Av.60 esq. 124 s/n, La Plata, 1900, Buenos Aires, Argentina
[c] YPF Tecnología S.A. (Y-TEC), Av. del Petróleo Argentino s/n e/ 129 y 143, Berisso, 1923, Buenos Aires, Argentina
[d] Departamento de Física, Facultad de Ciencias Exactas y Naturales, Universidad Nacional de La Pampa, CONICET, Uruguay 151, Santa Rosa, 6300, La Pampa, Argentina

ARTICLE INFO

Keywords:
Flowback
CFD-DEM
Multiphase flow
Hydraulic fracture

ABSTRACT

We present simulations using a coupled Computational Fluid Dynamics–Discrete Element Method (CFD–DEM) approach for a slurry of millimeter-sized particles in water which is squeezed between two walls and then made flow out though a narrow aperture. The process is akin to the flowback stage in the near wellbore zone of a hydraulic-stimulated well for hydrocarbon recovery. We consider different wall roughness and investigate its effect on particle production, final distance between walls, spatial particle distribution between the walls, and fluid production rate. We have found that the final distribution of particles changes significantly with small variations in the roughnesses of the walls. This in turn leads to production flow rates that may vary up to 50%. Although the main driver of the production for unconventional wells is the propped fracture network, these results suggest that the roughness of the fracture walls seems to play an important role in the final conductivity and therefore in the ultimate recovery.

1. Introduction

Hydraulic stimulation is used to speed up production in conventional and unconventional oil and gas reservoirs [Gandossi and Von Estorff (2015)]. This technique consists in injecting fluids at high pressure into the wellbore to induce fractures in the formation that later serve as highly conductive paths. To avoid fracture closure after hydraulic pressure release, the fracturing fluids contain granular materials that remain trapped in the fractures. Once packed, these granular materials (proppants) provide a porous media in the fracture through which hydrocarbons can flow [Economides (2000)]. During this process, many complex physical phenomena occur and a better comprehension of these allows the development of new technologies to improve the production efficiency. For that purpose, it is fundamental to gain a clear understanding of how the particles (grains) are transported, settled down and stabilized in order to avoid, or at least to diminish, undesirable effects such as pinch points (fracture closure near the wellbore isolating the well from the oil conductive channels), embedding (embedding the proppant grains in the formation) or flowback (destabilization and flow of proppant to the well during production) [Wang et al. (2018)].

Flowback is the process in which fluids are allowed to flow from the well following the stimulation treatment, either in preparation for a subsequent phase of treatment or in preparation for cleanup and putting the well into production. Only in USA, the total volume of shale gas flow back and produced water is about 50 billion gallons per year and seems to be increasing [Lyons (2014)]. During flowback, proppant particles rearrange in the fracture and some are produced to the well, causing damage in surface equipment during hydrocarbon production. The rearrangement of particles is a key factor during fracture closure and determine the production rate to some extent. Therefore, a better understanding of proppant rearrangement during fracture closure and flowback is particularly valuable.

Previous studies on proppant stability during flowback exist. Asgian et al. [Asgian et al. (1995)] have shown that hydraulic fractures propped with cohesionless, unbounded proppant fail under closure stress at a critical ratio of mean grain diameter to fracture width. They also identified the mechanism (arch failure) that triggers the mechanical instability and shown that the primary way in which drawdown affects proppant flowback (whenever the pressure gradient exceeds 75 psi/ft) is by transporting loose proppant grains in front of the stable arch to the

* Corresponding author. Universidad Tecnológica Nacional - Facultad Regional La Plata, Av.60 esq. 124 s/n, La Plata, 1900, Buenos Aires, Argentina.
E-mail address: manuel@iflysib.unlp.edu.ar (C.M. Carlevaro).

https://doi.org/10.1016/j.petrol.2021.108381
Received 19 May 2020; Received in revised form 22 August 2020; Accepted 6 January 2021
Available online 15 January 2021

wellbore. However, Asgian et al. did not consider the flow that occurs during the closure of the fracture but only after closure was completed. Mondal et al. [Mondal et al. (2016)] have studied the flow of particles and how they clog the perforation that connect to the casing. However, in their study there is not settling of the particles nor a closing of the fracture walls. In a different study, Shor and Sharma [Shor and Sharma (2014)] implemented a discrete element model to evaluate proppant pack stability and flowback where fracture walls are composed of spherical particles (a mean to introduce roughness to the walls). In this case, the model did not account the effects of the dragging fluids directly; instead they added a constant drag force to each grain to simulate the fluid drag. This study concluded that the final fracture width is unaffected by the initial fracture width (before flowback is initiated) if the proppant has the opportunity to be produced. Also, final fracture widths and proppant flowback are highly dependent on confining stress and the pressure gradient in the fracture.

In this work, we explore the flowback after stimulation by simulating a system of mono-dispersed particles which are placed in water and squeeze between two walls while the slurry is forced to flow through a small aperture on one edge of the slot formed by the walls (mimicking the perforation on the casing). In order to do so, we used the open source package CFDEM [Goniva et al. (2012)] which combines computational fluid dynamics calculations (CFD), which relies on the finite volume method to obtain numerical solutions to the Navier-Stokes equations, with classical discrete element method (DEM) code to calculate the motion of the particles. We have focused our attention on the spatial arrangement of the proppant particles during the settlement while there is a simultaneous flowback and a closure of the fracture. We consider different fracture wall roughness and show that this has a major impact on the final arrangement of the grains and the effective conductivity of the fracture.

The rest of the paper is organized as follows: In Section 2 we present a brief description of the particle–fluid flow model techniques used for the simulations. Section 3 is devoted to the validation of the technique by considering the hydraulic permeability of a proppant pack. In Section 4 we describe our model system for the study of flowback and the parameters we used to set up our simulation scheme. We present the main results in Section 5 and we analyze the sensibility of these results to the initial conditions and pressure gradient in Section 6. Finally, in Section 7 we present our conclusions.

2. Particle–fluid flow modeling techniques

A discrete element method (DEM), is a numerical technique for computing the motion of many interacting particles. The method considers a finite number of discrete particles (often with complicated geometries) interacting by means of contact and non-contact forces, where the dynamics of each particle is described by Newton's equations of motion.

Computational Fluid Dynamics (CFD) is a computer-based tool for simulating the behavior of systems involving fluid flow, heat transfer, and other related physical processes. It uses numerical analysis and data structures to solve the equations of fluid flow (the Navier–Stokes equations) over a region of interest, with specified conditions on the boundaries.

The discrete-based approach is typically represented by the combined approach of computational fluid dynamics and discrete element method (CFD–DEM) or the Lagrangian particle tracking (LPT). The latter can be thought as a simplified CFD–DEM model when the solid concentration is close to zero. In recent years, the coupled approach of CFD and DEM has been widely accepted as an effective tool to study pneumatic conveying and other particle–fluid systems. As an example, Baldini et al. [Baldini et al. (2018)] have used CFD-DEM to study the transport and settlement of proppant in a planar vertical cell that mimics a hydraulic fracture; considering different positions for the perforations and different proppant injection strategies. Using this same technique, Mondal et al. [Mondal et al. (2016)] have studied the bridging of a perforation during flow of particles dragged by a fluid through a single constriction in a rectangular channel.

In CFD–DEM, the solution of Newton's equations of motion for the discrete particles and the Navier–Stokes equations for the continuum fluid together with boundary and initial conditions will finally determine the mechanics of the solid and fluid phases. In practice, however, there are usually a large number of particles and a very large number of governing equations need to be solved for establishing the motion of each particle. Besides, the fluid field has to be calculated with a fine resolution to account for the detailed flow around particles. As a result, depending on the time and length scales of interest, simplifications have to be made to reduce the computational cost.

We carried out our simulations by using a CFD–DEM approach, coupling the fluid and solid phase through momentum exchange. The fluid phase is solved using the Finite Volume Method [Versteeg and Malalasekera (2011)] and the granular particles with DEM [Cundall and Strack (1979); Pöschel & Schwager (2010)]. The implementation used is the one provided by CFDEM [Goniva et al. (2012)], which couples LIGGGTHS [Kloss et al. (2012)] for the solid phase and OpenFoam-5.x for the fluid phase.

2.1. DEM

Each proppant particle is modeled as a "soft" sphere, and the motion of each particle is calculated by solving the Newton-Euler equations of motion for a rigid body [Pöschel & Schwager (2010)], which are then integrated over time to calculate the particle trajectories, i.e.,

$$m_i \frac{d^2\mathbf{r}_i}{dt^2} = \mathbf{F}_i^n + \mathbf{F}_i^t + \mathbf{F}_i^f + \mathbf{F}_i^b,$$
$$I_i \frac{d\boldsymbol{\omega}_i}{dt} = \mathbf{r}_{ic} \times \mathbf{F}_i^t, \tag{1}$$

where m_i and I_i are the mass and moment of inertia of the particle i. $\mathbf{F}^n$ and $\mathbf{F}^t$ are sum of the normal and tangential contributions, respectively, of all particle–particle and particle–wall contacts with particle i. The force exerted by the fluid phase on particle i is $\mathbf{F}_i^f$ and is generally expressed as $\mathbf{F}_i^f = \mathbf{F}_i^d + \mathbf{F}_i^p + \mathbf{F}_i^v$, where $\mathbf{F}_i^d$ is the drag force, $\mathbf{F}_i^p$ is the pressure force and $\mathbf{F}_i^v$ is the viscous force acting on the particles. Any other external force such as gravitational, electromagnetic, etc., is taken into account by $\mathbf{F}_i^b$ [Kloss et al. (2012)].

Two contacting spheres i and j (with radius R_i and Rj and centers at $\mathbf{r}_i$ and $\mathbf{r}_j$) experience a relative normal compression $\delta = |\mathbf{r}_{ij}| - d$, where $\mathbf{r}_{ij} = \mathbf{r}_i - \mathbf{r}_j$ and $d = R_i + R_j$. If $|r_{ij}| > d$ then there is no contact force. If $|r_{ij}| < d$, then we use the Hertzian contact model, where the normal push-back force between two overlapping spheres is proportional to the area of overlap of the two particles, and is a nonlinear function of the overlap distance. The contact force is given by [Silbert et al. (2001); Brilliantov et al. (1996) Zhang and Makse (2005)]

$$\mathbf{F} = (k_n \boldsymbol{\delta}_n - \gamma_n \mathbf{v}_n) + (k_t \boldsymbol{\delta}_t - \gamma_t \mathbf{v}_t)\,, \tag{2}$$

where $\boldsymbol{\delta}_n$ and $\boldsymbol{\delta}_t$ stands for normal and tangential overlap, and $\mathbf{v}_n$ and $\mathbf{v}_t$ stands for the normal and tangential components of the relative velocity of the surfaces of the two particles at the contact, respectively.

The stiffness and damping coefficients, k_n, k_t, γ_n, and γ_t can be expressed in terms of the material properties of the particles [Pöschel and Schwager (2010)] as follows:

Normal elastic constant: $k_n = \frac{4}{3}E\sqrt{R\delta_n}$

Tangential elastic constant: $k_t = 8G\sqrt{R\delta_n}$

Normal viscoelastic damping constant: $\gamma_n = -2\ln e\sqrt{\frac{5mE}{3(\ln^2 e + \pi^2)}}\sqrt[4]{E\delta_n}$

Tangential viscoelastic damping constant: $\gamma_t = -4\ln e\sqrt{\frac{5mG}{3(\ln^2 e + \pi^2)}}\sqrt[4]{E\delta_n}$

where R, m, E stands for the effective radius, mass, Young's modulus and Shear modulus and are defined as:

$$R = \frac{R_1 R_2}{R_1 + R_2};\ m = \frac{m_1 m_2}{m_1 + m_2};\ \frac{1}{E} = \frac{1-\nu_1^2}{E_1} + \frac{1-\nu_2^2}{E_2};$$
$$\frac{1}{G} = \frac{2(2-\nu_1)(1+\nu_1)}{E_1} + \frac{2(2-\nu_2)(1+\nu_2)}{E_2},$$

where R_i, m_i, E_i, G_i and ν_i (with $i = 1, 2$) stands for the radius, mass, Young's modulus, Shear modulus and Poisson's ratio of i-th particle respectively.

The first term in Eq. (2) corresponds to the normal force between the two particles and the second term is the tangential force. The normal force has two terms, a spring force and a damping force proportional to the relative velocity $\mathbf{v}_n$. The tangential force also has two terms: an elastic shear force (proportional to the tangential displacement vector $\boldsymbol{\delta}_t$) and a damping force (proportional to the relative velocity $\mathbf{v}_t$). The shear force has a "history" effect that accounts for the tangential displacement δ_t ("tangential overlap") between the particles for the duration of the time they are in contact. δ_t is obtained by integrating the surface relative velocity $\mathbf{v}_t$ during the elastic deformation of the contact. The magnitude of $\boldsymbol{\delta}_t$ is truncated as necessary to satisfy a local frictional yield criterion, $|\mathbf{F}_t| \leq \mu |\mathbf{F}_n|$, where μ is the particle–particle friction coefficient.

The material properties selected, for the Hertz contact model with tangential history and no particle–particle cohesion, are shown in Table 1. These properties are representative of typical proppant particles used in hydraulic stimulation operations (e.g., sand). The Young's modulus selected is lower than the actual values for sand in order to allow for a reasonable DEM time step and reduce CPU time. It has been shown that this lower Young's modulus has no significant impact on DEM simulations [Erta et al. (2001)].

The particle–wall interactions were modeled as particle–particle interactions. The geometry of the walls were created using Gmsh [Geuzaine and Remacle (2009)], which is an open-source 3D grid generator with a built-in CAD engine. This allowed us to vary the structure of the wall by introducing depressions and protuberances on their faces to create different roughness (see Section 4).

2.2. CFD

Fluid flows (gaseous or liquids) are governed by the Navier-Stokes equations which are based on the conservation laws of mass, momentum, and energy [Ferziger and Peric (2002); Pozrikidis (2011)].

Table 1
Values for material properties used in the simulations.

Coeff. of rolling friction:	$\mu_r = 0.5$
Poisson's ratio:	$\nu = 0.45$
Coeff. of restitution:	$e = 0.3$
Particle density:	2700 kg/m^3
Coeff. of friction:	$\mu = 0.5$
Particle Diameter:	$d_p = 1$ mm
Young's modulus	$E = 5$MPa

$$\frac{D\rho}{Dt} + \nabla\cdot\rho\mathbf{u} = 0, \quad \text{(Mass)}$$
$$\frac{D\rho\mathbf{u}}{Dt} = -\nabla p + \nabla\cdot\tau + \mathbf{F}, \quad \text{(Momentum)}$$
$$\frac{\partial\rho\mathscr{E}}{\partial t} + \nabla\cdot(\rho\mathscr{E}\mathbf{u}) = \nabla\cdot(k\nabla T + \tau\cdot\mathbf{u} - p\mathbf{u}) + \mathbf{u}\cdot\mathbf{F}. \quad \text{(Energy)}$$

These partial differential equations are the governing equations of CFD and jointly with boundary conditions and/or an equation of state, they fully describe the physical phenomena within the fluid. Loosely speaking, CFD is the art of replacing such system of partial differential equations by a set of algebraic equations which can be solved computationally.

The geometry and physical boundaries of the problem are defined using a CAD engine. Then, the fluid domain is divided into discrete cells (the mesh), where the physical model is defined with their respective initial and boundary conditions. The PISO algorithm (pressure implicit with splitting of operator), proposed by [Issa (1986)], solves the Navier-Stokes equations iteratively using the finite volume method. This discretization guarantees the conservation of fluxes through a particular control volume.

2.3. The CFD–DEM coupling equations

CFD-DEM coupling can be of two types, namely "unresolved" or "resolved", depending on the scale of the problem (i.e., the size of the particles and the level of resolution that is required for the flow field). Unresolved CFD-DEM is applicable to those cases where particle sizes are smaller than the CFD grid. In this case, the flow field around each particle is not resolved but the net effect on drag on the particles in each fluid cell is averaged. This method is widely used for industrial applications such as pneumatic conveying [Kuang et al. (2020)], slurry flow in pipelines [Lahiri and Ghanta (2010)], and many others problems due to the large number of particles involved in the simulations. However, it is important in the unresolved approach that one particle is smaller in volume than a fluid cell for the average effect of the fluid to be a good approximation. Resolved CFD-DEM is applicable to problems where particles are significantly larger than one fluid cell, which requires a large number of fluid cells to be used and this limits the total number of particles [Kloss et al. (2012); Mao et al. (2020)].

We perform our simulations using the unresolved scheme. The governing equations for the fluid phase, the so called Volume Averaged Navier Stokes Equations [Mondal et al. (2016)], for an incompressible fluid in this approach are:

$$\frac{\partial\alpha_f}{\partial t} + \nabla\cdot(\alpha_f\mathbf{u}_f) = 0,$$
$$\frac{\partial(\alpha_f\mathbf{u}_f)}{\partial t} + \nabla\cdot(\alpha_f\mathbf{u}_f\mathbf{u}_f) = -\alpha_f\nabla\frac{p}{\rho_f} - \mathbf{R}_{pf} + \nabla\cdot\tau. \quad (3)$$

The first equation stands for the fluid phase mass conservation equation for an incompressible fluid while the second stands for the momentum conservation equation for the fluid phase. Here, α_f is the volume fraction occupied by the fluid (recall that part of the volume is occupied by the solid particles), ρ_f is the fluid density, $\mathbf{u}_f$ is velocity of the fluid, and τ is the stress tensor for the fluid phase. $\mathbf{R}_{pf}$ represents the momentum exchange with the solid particle phase. This is calculated for each cell where it is assembled from the particle-based drag force, which depends on the particle volume fraction. For solving above-mentioned equations, a pressure-based solver implementing pressure velocity coupling (PISO) is used. The fluid is considered as Newtonian and the $k-\varepsilon$ turbulence model was adopted [Versteeg and Malalasekera (2011)]. The list of fluid properties used in our simulations are found in Table 2.

For numerical reasons, the momentum exchange $\mathbf{R}_{pf}$ is divided into implicit and explicit terms using the cell-based ensemble averaged

particle velocity $\mathbf{u}_p$

$$\mathbf{R}_{pf} = K_{pf}\left(\mathbf{u}_f - <\mathbf{u}_p>\right), \tag{4}$$

where

$$K_{pf} = \frac{\left|\sum_i \mathbf{F}_i^d\right|}{V_{cell}\left|\mathbf{u}_f - <\mathbf{u}_p>\right|}, \tag{5}$$

being $\mathbf{F}^d$ the fluid-particle drag force, which needs to be summed for all the particles in the cell of volume V_{cell}. There are many available models to calculate the drag force. We use the Di Felice drag correlation (see [Di Felice (1994); Zhu et al. (2007)]) in which the drag force on a given particle i is determined through

$$\mathbf{F}_i^d = \frac{1}{2}\rho_f\left(\mathbf{u}_f - \mathbf{v}_i\right)\left|\mathbf{u}_f - \mathbf{v}_i\right| C_d \frac{\pi d_p^2}{4}\alpha_f^{(2-\beta)}, \tag{6}$$

being $\mathbf{v}_i$ is the velocity of particle i, C_d the particle drag coefficient and β a model coefficient defined as

$$C_d = \left(0.63 + \frac{4.8}{Re_p}\right)^2, \quad Re_p = \frac{\rho_f d_p \alpha_f \left|\mathbf{u}_f - \mathbf{u}_p\right|}{\mu_f}$$
$$\beta = 3.7 - 0.65\exp\left[-\frac{\left(1.5 - \log Re_p\right)^2}{2}\right], \tag{7}$$

where Re_p stands for the Reynold's number and μ_f for the fluid dynamic viscosity.

In order to run the simulation we set the DEM time step at least an order of magnitude smaller than the CFD time step. Moreover, to ensure a good average for the unresolved approach we set the lateral size of the CFD cells to three times the particle diameter.

2.4. Validation: Darcy's law and hydraulic permeability

In the absence of gravitational forces, Darcy's law is a simple proportional relationship between the instantaneous flow rate through a porous homogeneously permeable medium of permeability k, the dynamic viscosity μ of the fluid and the pressure drop over a given distance [Muskat and Meres (1936); Muskat et al. (1937)]. For stationary, creeping, incompressible flow, in an isotropic porous media, Darcy's law takes the following form

$$\boldsymbol{q} = -\frac{\kappa}{\mu}\nabla p\,, \tag{8}$$

where $\boldsymbol{q}$ is the flux (volume discharged per unit time and per unit area) and ∇p is the pressure gradient vector. The negative sign is needed because fluids flow from high pressure to low pressure regions. This equation, for a fluid composed of a single phase, serves as the definition for the absolute permeability κ.

The validity of Darcy's law stands on the assumptions that the porous media is saturated, continuum, homogeneous and isotropic [Lambe and Whitman (1969)]. The upper bound validity in terms of Reynolds number is usually taken as $Re_p < 10$. In our simulations the porous media are packing of particles of diameter 1 mm. Therefore, the characteristic length L is taken as the mean grain size (1 mm in our case), which implies that the flux velocity have to be < 0.01 m/s to work at the low Reynolds numbers required.

Allen Haze [Hazen (1892)-Odong (2007)] derived an empirical formula for approximating the hydraulic permeability of a pack of granular material based on the effective diameter D_{10} (measured in m) of the grains,

$$\kappa = \frac{\mu C}{\rho g} D_{10}^2 \times 10^4, \tag{9}$$

where the Haze's empirical coefficient C takes a value between 0.0 and 1.5 in the literature, with an average value of 1.0 (Salarashayeri and Siosemarde [Salarashayeri and Siosemarde (2012)] usually take C between 1.0 and 1.5). If we use $C = 1$, for our reference 1 mm-particles, $\kappa \tilde{}$ $10^{-9}\mathrm{m}^2 = 1013$ D.

The aim of this section to validate our simulations by comparing the hydraulic permeability of a fracture packed with 1 mm size grains against the empirical estimate give by Eq. (9). For that purpose, lets considers the system depicted in Fig. 1. This is a slot of dimensions 7.5 mm in height, 22.5 mm in width and 2.5 mm in thickness filled with 200 spherical particles of diameter $d_p = 1$ mm and material density 2700 kg/m^3 (which corresponds to typical values for 16/30 mesh sand). The slot has a square perforation (side length 2.5 mm) at the bottom through which the fluid phase can flow while the particles are soon stopped by the formation of a blocking arch (see Fig. 1(a)). The contact force parameters, k_n, k_t, γ_n and γ_t were determined from the mechanical properties of the material as we mentioned in Section 2.1.

All the CFD domain was discretized with a structured mesh. The back face of the DEM domain is a *moving wall* that compacts the particle packing under a pressure of 172 kPa(~25 psi).[1] When the compression is done in the initial stage of the simulations some particles escape the slot until the blocking arch develops and a steady state of the flow is reached. After this steady state is obtained, the CFD domain is adjusted to match the DEM domain. The original thickness typically falls after compression to $\tilde{}2d_p$.

For the fluid phase we fixed the pressure difference Δp between the top of the domain (inlet) and the bottom perforation (outlet) so that $\nabla p - \rho \boldsymbol{g} = \frac{\Delta p}{L}$. We measure the flux in the outlet for several pressures drops once the system achieved the steady state.

In Fig. 1 we show a log-log plot of the pressure drop as a function of the flux. The lineal behaviour between $\boldsymbol{q}$ and Δp predicted by Eq. (8) is indeed validated since the slope for the log-log plot is 1.05. From the constant term in the fit we obtain that the permeability is $\kappa = 3445$ D $= 3.4 \times 10^{-9}$ m^2 (and the conductivity $K = \kappa \times$ fracture thickness $=$ 22604 mD.ft). These values can be compared with the prediction of Eq. (9) for which we obtained $\kappa \tilde{}$1000 D. Also, an extensive experimental study of proppant conductivity shows that for confining pressures below 2000 psi and 1 mm proppant particles $\kappa \tilde{}$932 D and $K \tilde{}$20000 mD.ft [Barree et al. (2018)]. The measurement of conductivity though proppant packs is in fact challenging since results are usually sensitive to details such as the protocol followed to prepare the proppant pack, the total amount of material used, etc. Having this in mind, the simulation approach followed here yields flows through porous media compatible with the empirical observations.

Table 2
Values for fluid physical properties.

Fluid density	$\rho = 1000$ kg/m^3
Dynamic viscosity	$\mu = 1 \times 10^{-3}$Pa.s
Kinematic viscosity	$\nu = 1 \times 10^{-6}$m^2/s
Turbulence parameter	$\varepsilon = 0.000765$ m^2/s^3

3. The model

We aim at modeling the flowback of a slurry composed of water and 16/30 mesh sand proppant in a region next to the casing perforation in a closing fracture. With this in mind we simulate approximately 12,000 spherical particles in water of diameter $d_p = 1$ mm which are initially randomly placed inside a vertical slot $52d_p$ high, $156d_p$ long and $2.5d_p$ thick (see Fig. 2). The slot has a rectangular perforation on the right for

[1] A more detailed description of the compression protocol used in the simulations can be found in the next section.

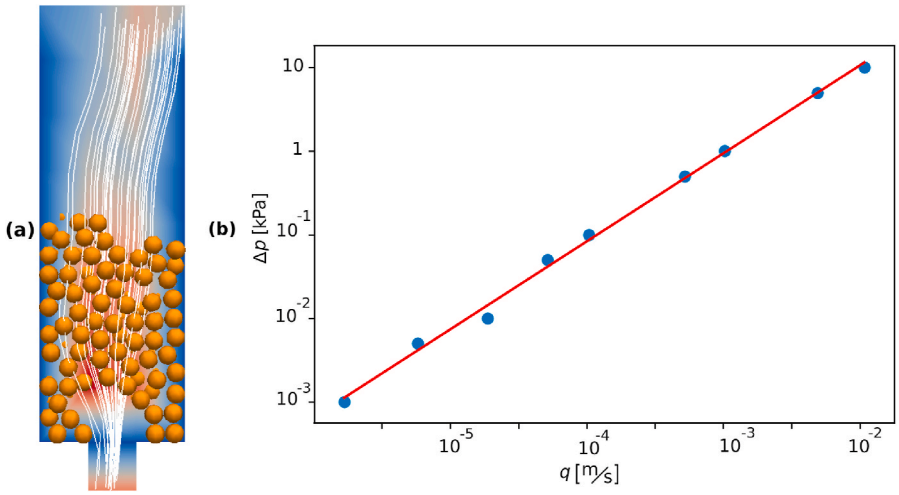

Fig. 1. (a) Snapshot of the simulated system. (b) Pressure drop as a function of the flux. The solid line corresponds the following exponential fit: $\Delta p = 1.35 \frac{MPa.s}{m} \times q^{1.05}$.

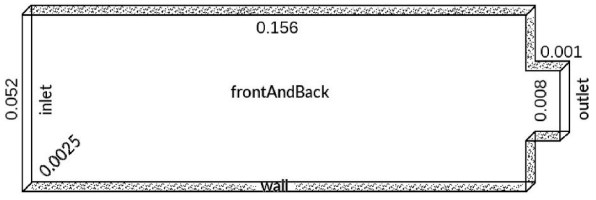

Fig. 2. Sketch of the simulation domain modeling a vertical fracture and a perforation (not to scale). Shaded faces correspond to impenetrable walls. In this drawing the perforation on the right is positioned at mid height.

the outflow of the slurry. This perforation is 8 mm in height, 1 mm in length and 2.5 mm in thickness; and can be positioned at two alternative heights: *bottom* (leaving a gap of 4 mm from the base of the cell), or *middle* (centered at mid height of the slot). On the left side, the entire height of the slot acts as an inlet that allows the fluid phase (not the particles) to flow in. This effective left wall for the particles simulates the effect of other particles beyond the domain on the left which will prevent grains in the cell to flow to the left.The material properties that define the behaviour of the fluid and the particles are set as discussed in Section 2.

We generate roughness on the side walls (front and back in Fig. 2) using square pyramids of base 1.0×1.0 mm^2 and height 1 mm that either protrude or depress the wall surface, except for the random case where the pyramids height randomly varies from one to another in the range -1.0 mm to 1.0 mm. The bases of these pyramids are arranged to tile the side walls (an example can be seen in Fig. 3). The front and back walls in any given simulations have complementary roughness so that the protruding pyramids in the front wall fit in the depressing pyramids of the back wall and *vice versa*, maintaining the width of the fracture

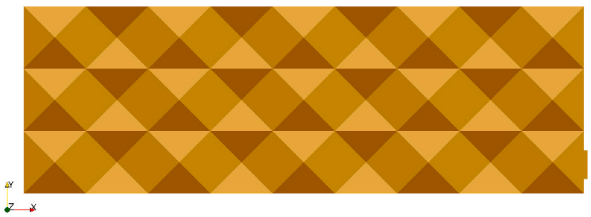

Fig. 3. Example of checkerboard roughness on a side wall made by decorating a flat wall with alternating protruding and depressing pyramids. In this drawing the perforation on the right is placed at the bottom position.

constant everywhere. We use five different arrangements for the pyramids to construct different types of roughness (see Fig. 4):

- Planar: No roughness.
- Horizontal: Protruding (depressing) pyramids are aligned along the horizontal direction.
- Vertical: Protruding (depressing) pyramids are aligned along the vertical direction.
- Checkerboard: Protruding and depressing pyramids are alternated.
- Random: The height of the pyramids was randomly selected between -1.0 mm and 1.0 mm.

The back wall was simulated as a *moving wall* that allowed us to mimic the closure of the fracture and study how final distribution of particles affect the conductivity. The back wall compresses the system by moving at a constant velocity until the closure pressure reaches a target value of 345 Pa(˜0.5 psi). Although, the maximum closure pressure achieved in this study is much lower than the expected closure pressure at the subsurface for a typical unconventional reservoir, it was enough to generate the proppant re-arrangement needed for the aim of this work. Additional phenomena such as embedment or the spalling in fractures were not taken into account in this work and others simulations would be required to get some conclusions in that way.

As we stated in Section 2.3, we solved the Navier-Stokes equation for an incompressible Newtonian fluid (water). The CFD domain was discretized with a structured mesh generated with 2113 quadrangles. We set a constant pressure p boundary conditions and null velocity gradients in the x-direction in the inlet and outlet face with the following protocol:

- Initial stage: during the initial 0.5 s we impose a uniform pressure field P_{init} along the slot in order to let particles to settle and get trapped by the *moving wall.* In this stage there is no pressure gradients apart from the one established by gravity. The only flow of the fluid phase is induced by the hydrodynamic effect of the settling particles in the slot.
- Transitory stage: from 0.5 s to 1 s the pressure difference between the inlet and outlet faces is increased at a constant rate to finally reach 1 kPa (˜0.14 psi). This pressure gradient induce the flowback of the slurry.
- Stationary stage: the 1.0 kPa pressure drop is kept constant up to the end of the simulation.

Additionally, we set a no-slip boundary condition on the top and bottom boundaries. We modeled the fluid as two-dimensional using

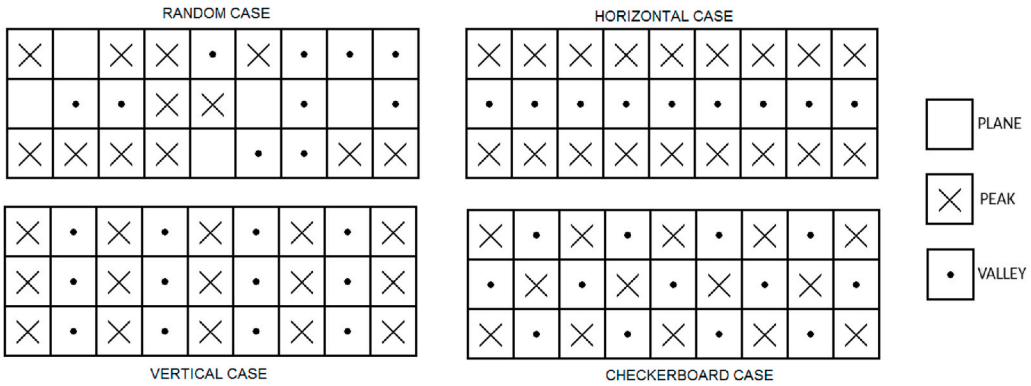

Fig. 4. Types of roughness simulated for the front and back walls of the cell. For the random case the height of the pyramids is random, for the other cases all pyramids are 1.0 mm in height (either −1.0 mm or 1.0 mm).

symmetric boundary conditions on the front and back planes. This means that the effect of these walls on the fluid is not accounted for. This is a limitation of the unresolved method since the prescription for getting accurate results is that the mesh cell size to particle size ratio should be approximately 5 : 1 [Kuruneru et al. (2019)] (there is not full agreement among the research community regarding the preferred ratio; values vary in literature). Taking into account that our system is $2.5d_p$ thick we cannot divide the slot thickness into several fluid cells to calculate a detailed velocity profile.

The boundary conditions on the pressure field was selected to achieve a flow velocity at the perforation that mimics the estimations that can be extracted from the data reported in the field. An estimation based in a well that produces 90 m^3/day of fluids through 1026 active perforations of diameter 0.0072 m, leads to a mean flow velocity of 0.025 m/s at each perforation. This is an estimate for the total oil and water produced during the first days after well completion. However, this number is subject to various assumptions. On the one hand, it depends on how many fractures are considered as active and how many perforations connect each fracture to the casing. On the other, the production per day decreases during the life time of the well. In the literature values of 0.1 m/s [Mondal et al. (2016)] are considered. We run our simulations adjusting the pressure gradient in the slot to reach a value of 0.9± 0.3 m/s which represents a worst case scenario. In section 5.3 we studied the effect of this flow velocity on the results reported.

The time step for the DEM calculation was set to 10^{-5} s to achieve acceptable values of the Raleight and Hertz time. It is recommended to pick a DEM time step not longer than 10% of the Raleight and Hertz time to properly model particle–particle and particle–wall interaction [Washino et al. (2016)]. The coupling time is set to 100 times the DEM time step. The time step for the CFD calculations must be equal to, or smaller than, the coupling time. Moreover, to ensure a synchronous run, the coupling time should be a multiple of the CFD time step. With this in mind we set the CFD time step to 5×10^{-5} s.

It is worth remarking that the selected CFD time step satisfies the Courant-Friedrichs-Lewy (CFL) condition in order to maintain numerical stability [Hirsch (2007)]. For a one dimensional flow, the CFL coefficient C is defined as

$$C = u\frac{\Delta t}{\Delta x},$$

where u is the fluid velocity, Δt is the time step and Δx is the mesh size. Following other authors recommendations, it is advisable to keep $C <$ 0.5 to obtain accurate results on the fluid velocity and pressure field [Mondal et al. (2016)].

We carried out a total of 36 simulations that can be classified as follows:

- 10 simulations exploring the five types of roughness and the two positions for the perforation.
- 4 simulations with different initial particles positions for a given wall roughness and given perforation position. This constitutes a test for the sensitivity to initial conditions of the particles.
- 10 simulations with different random wall roughness (different random seeds) for a fixed initial distribution of particles and perforation position. This allowed to test the sensitivity to the specific roughness created during stimulation treatments.
- 12 simulations with different pressure gradient between the inlet and outlet side for both smooth and rough walls. This constitute a test for the sensitivity to the boundary conditions of the fluid.

4. Results

4.1. Smooth walls

In Fig. 5 (left column), we show the spatial distribution of the packing fraction (fraction of volume occupied by the particles) in a slot with smooth walls at different stages of a simulation with the outlet perforation placed in the bottom position. The packing fraction profiles allows for a simple averaged visualization of the particle concentration. Blue areas in these images indicate that there are no particles present in this part of the slot. Fig. 5(a) shows the initial configuration where particles are placed homogeneously distributed across the system. Fig. 5 (b) corresponds to the final stage of settlement and fracture closure. In Fig. 5(c) the pressure drop and the flowback is being established (at this point only half of the final pressure gradient has been established). As we can see, the flow has dragged a small portion of the settled particles close to the perforation zone. Fig. 5(d) shows the final state after a long flowback period. The erosion of the particles next to the outlet creates a significant void. This is consistent with the observations in ref. [Shor and Sharma (2014)]. The right column in Fig. 5 shows the corresponding fluid velocity profiles to the images in the left column. Once the flow is fully developed (see part (d)), most of the fluid flows towards the outlet from the upper region of the cell above the dune of particles.

In Fig. 6(a), we plot the width of the fracture as a function of time for a smooth wall comparing simulations with the middle (blue) and the bottom (orange) perforation position. In the inset to Fig. 6(a), we zoom into the initial part where the slot closure occurs. We note that the initial closure, before the flow is turned on, proceeds in a similar way for both outlet placements yielding similar final fracture widths. However, during the establishment of the pressure gradient in the cell (0.5 − 1.0 s) more particles are eroded with the perforation placed at the bottom (see Fig. 6(b)) and the walls are able to close further. Although the bottom perforation retains less grains which leads to a slighter narrower fracture, the fluid flow is not affected. Indeed, Fig. 6(c) shows that the fluid velocity at the perforation is virtually the same in both perforation

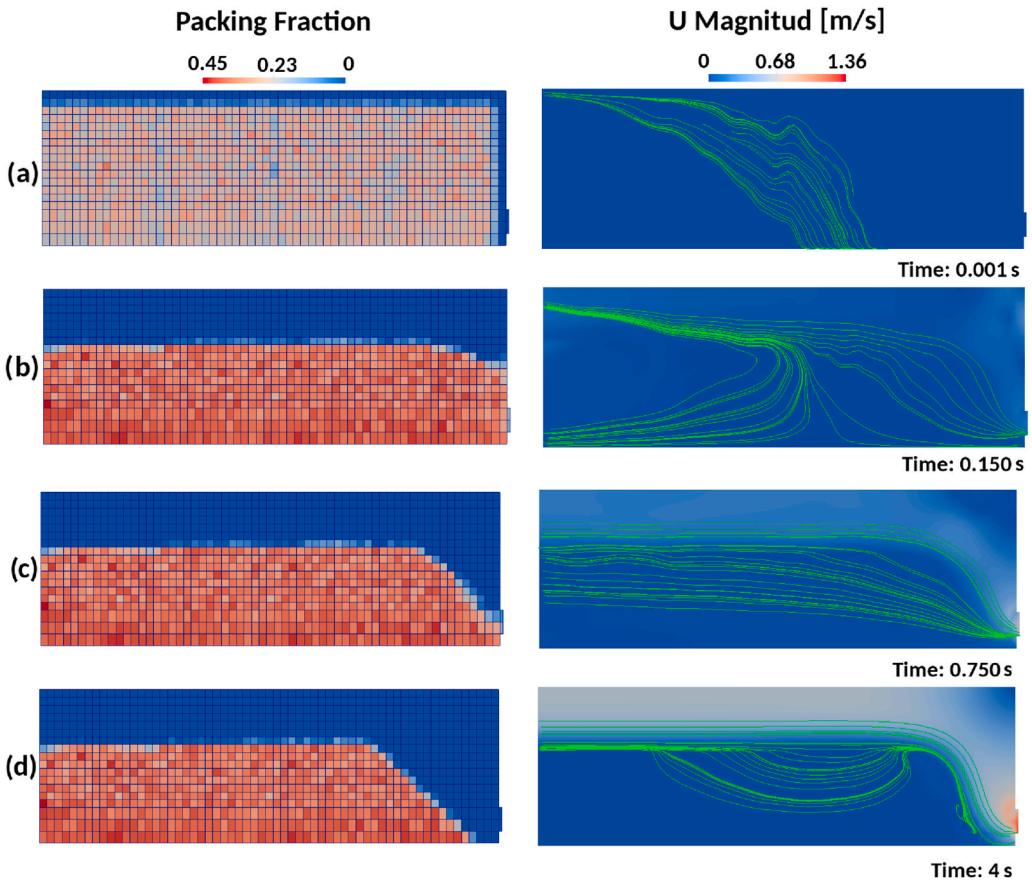

Fig. 5. Heatmap of the local packing fraction for a simulation with smooth walls and bottom perforation (left) and the corresponding profile of the modulus of the fluid velocity and stream lines (right). Different times correspond to different phases along the simulation: (a) initial configuration, (b) after fracture closure and particle settling, (c) during establishment of pressure drop and flow stabilization, (d) final configuration.

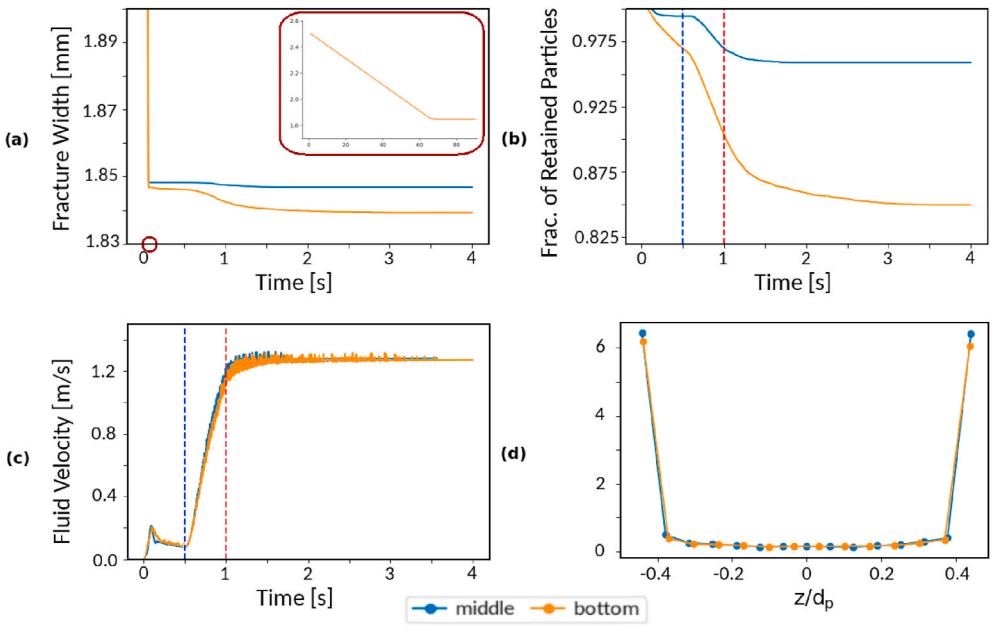

Fig. 6. Fracture width (a), fraction of retained particles (b) and fluid velocity at the perforation (c) as a function of time for flowback simulations with smooth walls. The blue and orange curves correspond to the middle and bottom placement of the perforation, respectively. The vertical dashed blue and red lines indicate the start and end of the pressure ramp when the flow is turned on. (d) Probability distribution function of the particle z-position (i.e., perpendicular to the fracture plane) after the fracture closure and particle settlement. (For interpretation of the references to colour in this figure legend, the reader is referred to the Web version of this article.)

positions. This can be attributed to the void created in front of the dune (see Fig. 5). The fluid phase finds its path though the upper region of the slot and down across the void next to the well, which is present for both perforation positions.

In Fig. 6(d), we plot a histogram of the particle distribution in the z-axis (i.e., perpendicular to the fracture walls) within the dune at the end of the simulation. The distribution shows two peaks, each of them at 0.5 mm from the center of the slot. This indicates that the grains arrange in a

bi-layer in any of the two ways we place the outlet perforations.

4.2. Rough walls

In this section we focus on the effect that the roughness of the inner walls of the fracture has on the arrangement of particles after flowback and on the effective permeability of the fracture itself. We run eight simulations varying the roughness structure (horizontal, vertical, checkerboard, and random) and the placement of the perforation (see Section 4).

In Fig. 7(a), we plot the fracture width as a function of time. Like in the smooth walls case, the fracture closes and pack the particles in a short time, after which the fracture width remains essentially constant. While for smooth walls we observed that the placement of the outlet perforation affects the final width of the fracture, in all rough fractures we found the same final fracture width for both low and mid height position of the perforation. For the vertical, horizontal and checkerboard roughness, we obtain about the same final fracture width as for smooth walls. However, the random roughness leads to a 4% wider fracture.

In Fig. 7(b), we plot the fraction of retained particles during the simulation for different rough walls and outlet placement. With the exception of the random roughness case, every rough wall develops a major eroded area near the perforation when it is placed at the bottom of the fracture. We do not show the packing fraction profiles since they are similar to the ones shown in Fig. 5 for smooth walls. The difference in particles retained between the middle and bottom perforation is much narrower than the difference observed with smooth walls (see Fig. 6(b)). We find a peculiar behaviour for random roughness in which a bottom perforation is able to retain more particles than a mid height perforation. This can be explained comparing the final packing fraction distribution between the middle and bottom perforation position (see Fig. 8). As we can see, the particles clogged the outlet in the bottom placement before a large number of grains could flow through the well. For the mid height outlet no clog developed and a larger number of particles was able to exit the cell. Clogging is an statistical process (see for example [Zuriguel et al. (2015); Zuriguel (2014); Mondal et al. (2016)]) and therefore different realizations of a simulation can lead to clogs being developed either sooner or later than this particular realization. In the next section we will pursue this phenomenon further.

Fig. 8 shows that rough walls generate an irregular packing fraction distribution inside the proppant dune, with vacancies and high concentration zones along the slot. This is in contrast with the uniform distribution of particles that we found for smooth walls in Fig. 5(d). These more open heterogeneous structure for rough walls allow a much deeper penetration of the flow stream lines intro the sand bed.

Fig. 9(a) shows the mean fluid velocity as a function of time for the various roughness and placement of the perforation. Here we can observe that the mid height outlet can have up to double the fluid

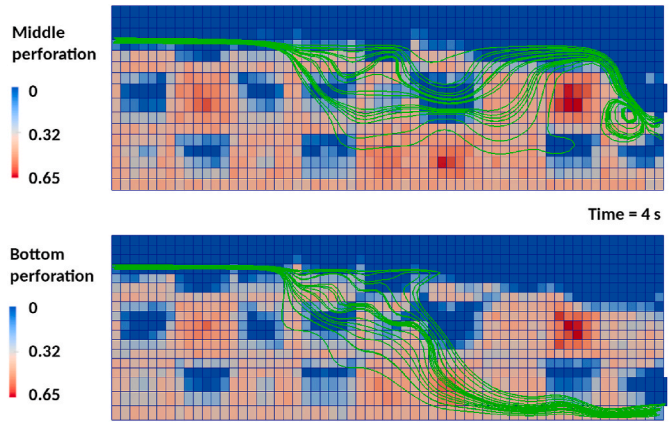

Fig. 8. Packing fraction distribution for the final state for the random roughness for middle and bottom perforation location. Green lines correspond to streamlines. (For interpretation of the references to colour in this figure legend, the reader is referred to the Web version of this article.)

velocity attained for the same roughness but using a bottom outlet. This is in contrast with the smooth walls that showed not difference in outflow velocity for low and mid height outlets. It is worth nothing that for the mid height outlet the spread in flow velocity is narrow, whereas for the bottom outlet the spread in fluid velocities is much wider. Again, this is related to the fact that the bottom outlet eventually clogs during simulations and the flow of the fluid though this clog of particles strongly depends on the actual arrangement of the grains. In contrast, for the mid height outlet, the region close to the outlet is effectively vacated from particles and the fluid is directly transported from the region of the cell above the particle dune with no significant obstacles.

In Fig. 9(b), we plot the particle distribution in the z-direction. It is possible to distinguish a big difference between the random roughness walls and the rest of the roughness structures explored. Indeed, the random roughness walls present two well defined peaks in the particle distribution separated by roughly 0.5 mm. This resembles the distribution found in the smooth wall simulations (which has been included in Fig. 9(b) for reference). Other cases with different roughness show a much more spread distribution (about $3d_p$ wide) with only one maximum at the center of the slot width. As in the smooth walls case, the two peaks for the random roughness can be interpreted as a hint of a typical profile of a bi-layer of grains. However, this bi-layer is not as well defined as for the smooth wall simulations. As in the smooth wall case, there is no appreciable difference in the z-distribution of particles between the bottom and middle perforation. For this reason we have only included the distribution for the bottom outlet.

Finally, in Table 3, we have computed the permeability κ and the conductivity K for all types of walls, both for middle and bottom

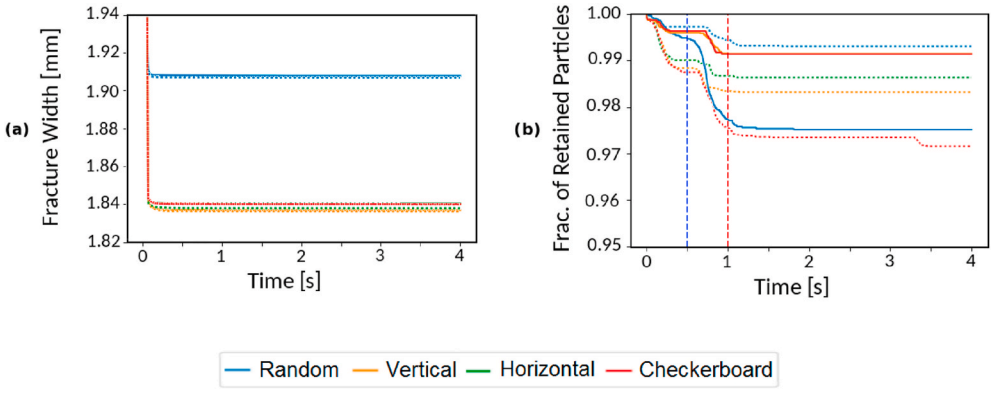

Fig. 7. Fracture width (a) and fraction of retained particles (b) as a function of time. Full and dashed lines correspond to middle and bottom perforation position, respectively. The continuous green line is indistinguishable from the red one in the right hand side plot. The vertical dashed blue and red lines indicate the start and end of the pressure ramp when the flow is turned on. (For interpretation of the references to colour in this figure legend, the reader is referred to the Web version of this article.)

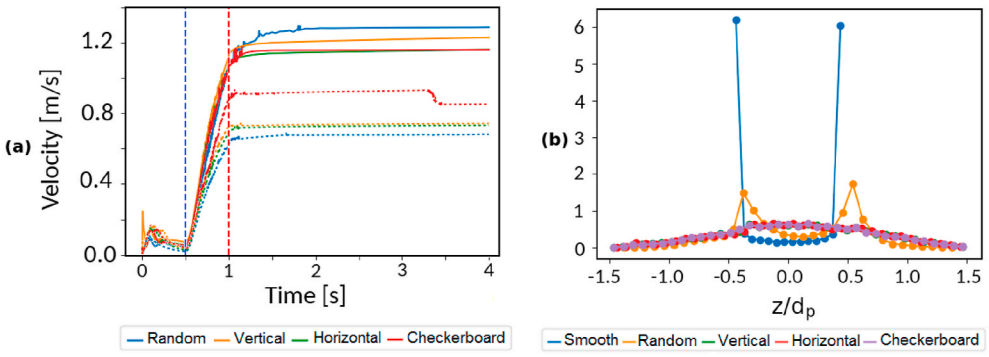

Fig. 9. (a) Fluid velocity at the perforation as a function of time. Full and dashed lines correspond to middle and bottom perforation case, respectively. (b) Profile of particle distribution in the z-direction, after the fracture closure and particle settlement for the bottom perforation. The vertical dashed blue and red lines indicate the start and end of the pressure ramp when the flow is turned on. (For interpretation of the references to colour in this figure legend, the reader is referred to the Web version of this article.)

Table 3
Final permeability κ and conductivity K for bottom and middle perforation for all types of fracture walls.

	Bottom Perforation		Middle Perforation	
	κ [D]	K [D.ft]	κ [D]	K [D.ft]
Smooth	31,005	187	31,318	190
Random	16,618	103	31,362	196
Vertical	18,110	109	29,955	181
Horizontal	17,857	107	28,287	171
Checkerboard	20,758	125	28,261	171

perforation in the final steady state of the simulation. The permeability was computed as $\kappa = \mu v_{\text{mean}} L/\Delta p$, where v_{mean} is the mean velocity of the fluid phase in the slot and L is the length of the slot. For all rough walls and bottom perforation we find values of K in fair agreement with laboratory experiments (see for example Barree et al. (2018) for 16/30 sand at low closure pressures). However, we have to pay special attention to the fact that the upper region of the fracture is not propped by particles and this creates a channel that ease the flow towards the perforation. Only a small region of the proppant dune close to the perforation needs to be crossed by most of the fluid (see streamlines in Fig. 8 for the bottom perforation). This may cause the effective permeability of the fracture to be higher than for a uniformly filled slot, as is usually considered in conductivity laboratory tests. For the perforations placed at mid height, the conductivity of all rough wall fractures is much higher (see right columns in Table 3). This seems to be caused by the lack of proppant next to the perforation (see Fig. 8 for the middle perforation). For smooth walls, irrespective of the position of the perforation, the flowback washes away all particles near the perforation and therefore the fluid has a free path to the perforation. This makes the smooth wall fracture to have a higher effective conductivity.

Despite the values obtained for the conductivity of the propped fractures, it is important to mention that the flux does not follow a simple linear relation with the pressure drop. This is connected with the fact that the particles do not fill the fracture homogeneously. Therefore, the conductivity values cannot be used to extrapolate flux linearly for other values of the pressure drop. In the next section we discuss this in more detail.

4.3. Pressure drop

The aim of this section is to study the effect of the pressure drop imposed to drive the flow in the slot on the velocity of the fluid phase at the perforation. For that purpose we carried out six simulations with different pressure gradients for the smooth walls and for the random rough walls placing the perforation at the bottom. We found that the pressure drop has almost no incidence in the distribution of particles in the z-direction (distributions are indistinguishable from those shown in Fig. 9(b)). This is to be expected since we let particles to settle and get trapped by the moving wall before we set the pressure drop in the slot.

In Fig. 10, we plot the fraction of retained particles for smooth and random rough walls as a function of time for bottom perforation. Here, we observe that roughness has a deep impact in the final number of retained particles when the pressure drop is changed. On the one hand, for the smooth walls, the fraction of particles retained fall as the pressure drop is increased. This is consistent with a larger fluid velocity in the fracture that can drag more particles trough the perforation. On the other hand, for random rough walls, there is almost no significant change in the particles retained when the pressure drop is increased (note the change in the vertical scales in part (a) and (b) in Fig. 10). It seems that the rough walls can effectively hold the particles much more efficiently even when the pressure drop increases.

Fig. 11 shows the fluid velocity at the outlet for smooth and random rough walls as a function of the pressure drop in log-log scale. As we can see, the exit fluid velocity does not scale linearly with Δp. For the smooth walls the fluid velocity scales as $v_{out} \propto \Delta p^{0.56}$, whereas for the rough walls we obtain $v_{out} \propto \Delta p^{0.83}$. It is important to emphasize at this point that these scalings are not expected to contitute a verification of the Darcy's law. During flowback, the arrangement of the pack of grains is different for each Δp. Therefore the flux obtained for a given Δp corresponds effectively to a different porous structure than the flux measured at a different Δp. In the more realistic case of the rough walls, one can conclude that the sub-linear exponent indicates a clear reduction of efficiency when the pressure drop is increased. Therefore, if pumping is required, one should consider that increasing the pressure drop will not necessarily increase proportionally the flow rate.

5. Sensibility to initial conditions

We assume that the random rough walls are the more realistic of the cases studied here. However, the actual realization of the random roughness can have an impact on the effective flow during flowback and production. Also different realizations of the simulations with the same random rough wall can yield slightly different results if the initial random positions of the particles are different. In order to explore these effects on the simulation results, we carried out a series of additional simulations for random rough walls with the bottom perforation configuration.

5.1. Initial distribution of particles

For a fixed random rough wall, we performed four simulations with different initial positions of the particles in the slot. The particles were always uniformly distributed for the initial configuration, but the random seed used was varied. The z-distribution in all the cases resulted indistinguishable from the one plotted in Fig. 9(b). In Fig. 12 we plotted the fraction of retained particles and the fluid velocity at the outlet as a function of time. We observe that the flow at the outlet can vary up to 25%. This would imply that if a fracture is producing at a low rate,

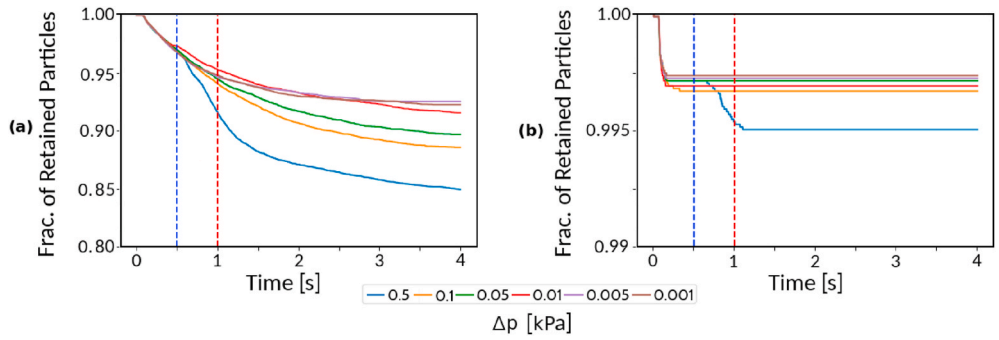

Fig. 10. Fraction of retained particles for smooth (a) and random rough (b) walls. Note the different vertical scales. The vertical dashed blue and red lines indicates the start and end of the pressure ramp when the flow is turned on. (For interpretation of the references to colour in this figure legend, the reader is referred to the Web version of this article.)

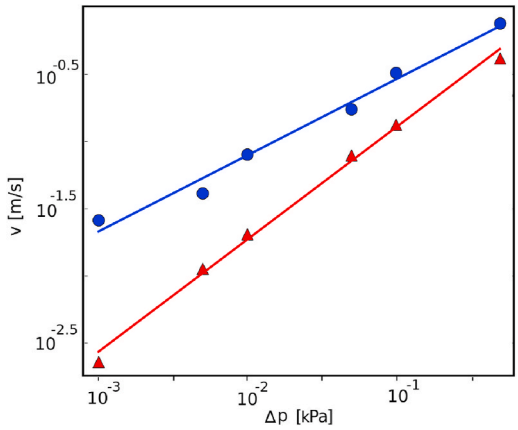

Fig. 11. Fluid velocity v_{out} as the perforation as a function of the pressure drop Δp for smooth (blue spot) and random rough walls (red triangles) for bottom perforation. Lines corresponds to linear fits. For the smooth walls we obtain $v_{out} \propto \Delta p^{0.56}$, and for the rough walls $v_{out} \propto \Delta p^{0.83}$. (For interpretation of the references to colour in this figure legend, the reader is referred to the Web version of this article.)

opening and closing the fracture again may lead to rearrangements in the proppant pack that can improve somewhat the production. This is valid only if the flow rate is mainly limited by the proppant pack close to the perforation and not other limitations upstream in the fracture.

5.2. Realization of the random roughness

We carried out six simulations with random rough walls where the seed to build the random pyramids is varied. In Fig. 13, we plot the fraction of retained particles and the fluid velocity at the outlet as a function of time. It is interesting to observe how the particular realization of the wall roughness affects the exit fluid velocity which is proportional to the effective conductivity of the fracture. The final fluid velocity varies as much as 50% when the roughness realization changes (see 13(b)). This variability is double that of the one observed for different initial particle positions. Of course, the wall roughness cannot be altered easily once a fracture has been created. Therefore, we cannot foresee any simple solution to improve production in a low productivity fracture. However, this result can provide a plausible explanation for the large variability in production of stimulated wells. Even when different wells are stimulated following the same protocols, the precise structure of the roughness of the fracture walls created cannot be controlled. This small changes in the fracture walls can lead to at least 50% changes in the production of two nearby wells even if treated alike.

Fig. 13(a) indicates that the realizations of wall roughness that retain less particles during flowback are the ones that yield a larger final fluid velocity at the perforation. In general, one expects that a poor retention be associated to a loss of fracture conductivity. However, this does not seem to be the case in our simulations. In Fig. 14, we show the packing fraction for different random realizations of the roughness. As we can see, the realizations that lead to high outflow ((a) and (b)) correspond to the ones that leave a clear path that connects the upper part of the fracture to the perforation. The roughness that yields the lowest outflow presents a thick region of proppant above the position of the perforation that partially blocks the flow from the upper (unpropped) region of the fracture.

6. Conclusions

We modeled the fluid flow and proppant rearrangement in a fracture close to the perforation during the flowback stage in a stimulated hydrocarbon formation. For this we have used the CFD–DEM approach. The slurry modeled consisted of 1 mm sized spherical particles in water

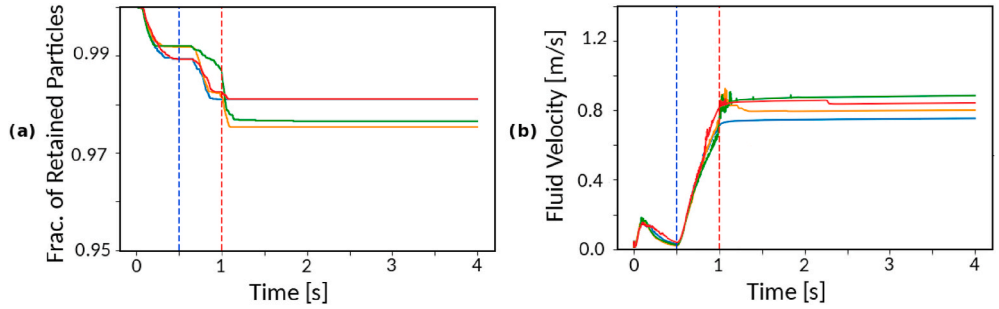

Fig. 12. Fraction of retained particles (a) and fluid velocity at the outlet (b) as a function of time for four different initial positions of the particles and a given realization of the random roughness of the walls. The outlet is placed at the bottom. The vertical dashed blue and red lines indicate the start and end of the pressure ramp when the flow is turned on. (For interpretation of the references to colour in this figure legend, the reader is referred to the Web version of this article.)

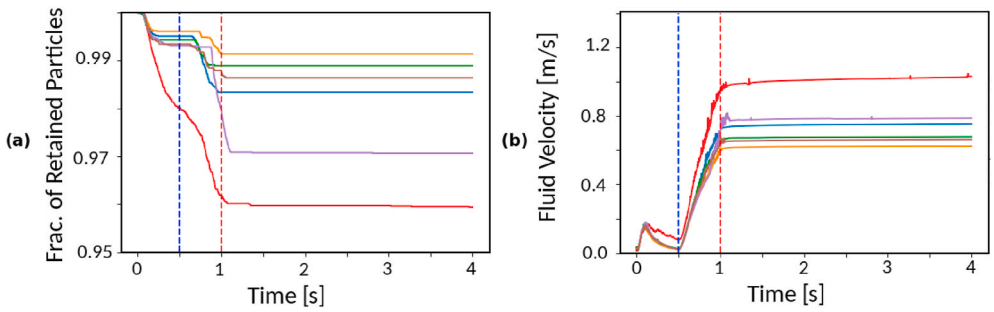

Fig. 13. Fraction of retained particles (a) and fluid velocity at the outlet (b) as a function of time for six different random rough walls. The outlet is placed at the bottom.

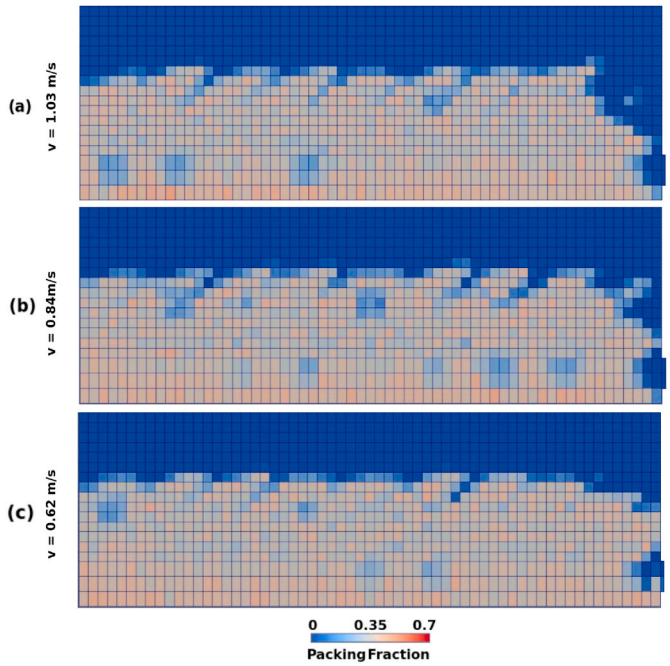

Fig. 14. Final packing fraction profile for three different random realizations of the rough walls. (a) and (c) have the same initial distribution of particles, while (b) has different initial particle distribution. In all cases the pressure drop was set to 1 kPa and the perforation is placed at the bottom. The final fluid velocity at the perforation is: 1.03 m/s (a), 0.84 m/s (b) and 0.62 m/s (c).

which was squeezed between two walls and then made to flow out though a narrow aperture (the perforation) by setting a pressure drop Δp. We carried out a total of 36 simulations varying the roughness of the walls, the positions of the perforation, the initial condition of the proppant suspension, and Δp. In each simulation we considered the particle retention (inverse to the proppant production to the well), final distance between walls, spatial distribution of the particles and the fluid phase flow rate.

We have shown that the particles arrange themselves in the fracture as a bi-layer. This is so for smooth walls and for random rough walls. In the case of smooth walls the two layers are clearly more distinguishable. for the more artificial roughness explored the z-distribution is peaked at the center. This distributions are not affected by the location of the perforation (bottom or middle) nor by the pressure drop used to set the flow. For the vertical, horizontal and checkerboard roughness we obtain about the same final fracture width as for smooth walls (1.84 mm). However, the random roughness leads to a 4% wider fracture. Using a perforation placed at the bottom leads to the ejection of more particles than the use a a mid height perforation. However, the bottom perforation is more prone to clogging. The distribution of proppant on the plane of the fracture is very heterogeneous for rough walls with large areas vacated in particles. For smooth walls, however, the distribution is rather homogeneous.

We have seen that the flow rate (i.e., or the fluid velocity at the perforation) does not grow linearly with the pressure drop. The actual exponent for the random rough walls is about 0.8. This implies that increasing the pressure drop (for instance by pumping) will not yield a proportionally higher production rate.

The use of different initial positions for the particles may induce significant variations in the final flow rate (up to 25%). These changes are stochastic since the initial distribution used is homogeneous in all simulations and only the random seed for the particle positions is varied. This is, for the same fracture, rearrangements of the grains close to the perforations make a significant impact on the flow rate. Therefore, if a fracture is producing at a low rate, shortly opening and closing the fracture may lead to rearrangements in the proppant pack that could improve somewhat the production.

Finally, we have found that for a random rough wall, the final production flow rate may vary up to 50% depending on the actual random realization of the roughness. These stochastic variations in the details of the wall roughness is a plausible explanation for the well known dispersion in hydrocarbon production for equally treated wells in the field. This fact can help to understand the differences in productions of nearby wells which, being treated in the same way, are expected to have similar production rates.

Credit author statement

F.G.V., C.M.C., M.S. and L.A.P. contributed to the design and implementation of the research, to the analysis of the results and to the writing of the manuscript.

Declaration of competing interest

The authors declare that they have no known competing financial interests or personal relationships that could have appeared to influence the work reported in this paper.

Acknowledgment

This research was funded by CONICET and Y-TEC SA. The authors would like to acknowledge Dr. Mauro Baldini for his fruitful technical assistance provided during the initial stages of the study.

References

Asgian, M., Cundall, P., Brady, B., 1995. The mechanical stability of propped hydraulic fractures: a numerical study. J. Petrol. Technol. 47, 203–208. URL. http://www.onepetro.org/doi/10.2118/28510-PA. doi:10.2118/28510-PA.

Baldini, M., Carlevaro, C.M., Pugnaloni, L.A., Sánchez, M., 2018. Numerical simulation of proppant transport in a planar fracture. A study of perforation placement and injection strategy. Int. J. Multiphas. Flow 109, 207–218. https://doi.org/10.1016/j.

ijmultiphaseflow.2018.08.005. URL. https://linkinghub.elsevier.com/retrieve/pii/S030193221830051X.
Barree, R.D., Miskimins, J.L., Conway, M.W., Duenckel, R., 2018. Generic correlations for proppant-pack conductivity. SPE Prod. Oper. 33, 509–521. URL. http://www.onepetro.org/doi/10.2118/179135-PA. doi:10.2118/179135-PA.
Brilliantov, N.V., Spahn, F., Hertzsch, J.-M., Pöschel, T., 1996. Model for collisions in granular gases. Phys. Rev. 53, 5382–5392. https://doi.org/10.1103/PhysRevE.53.5382. URL.
Cundall, P.A., Strack, O.D.L., 1979. A discrete numerical model for granular assemblies. Geotechnique 29, 47–65. https://doi.org/10.1680/geot.1979.29.1.47.
Di Felice, R., 1994. The voidage function for fluid-particle interaction systems. Int. J. Multiphas. Flow 20, 153–159. https://doi.org/10.1016/0301-9322(94)90011-6. URL. https://linkinghub.elsevier.com/retrieve/pii/0301932294900116.
Economides, M.J., 2000. Reservoir Stimulation, third ed. Wiley, Chichester, England ; New York.
Ertaş, D., Grest, G.S., Halsey, T.C., Levine, D., Silbert, L.E., 2001. Gravity-driven dense granular flows. Europhys. Lett. 56, 214–220. https://doi.org/10.1209/epl/i2001-00508-7. URL. https://iopscience.iop.org/article/10.1209/epl/i2001-00508-7.
Ferziger, J., Peric, M., 2002. Computational Methods for Fluid Dynamics. Springer Berlin Heidelberg, Berlin, Heidelberg.
Gandossi, L., Von Estorff, U., 2015. European Commission, Joint Research Centre, & Institute for Energy and Transport (2015). An Overview of Hydraulic Fracturing and Other Formation Stimulation Technologies for Shale Gas Production. Technical Report Publications Office of the European Union. URL. http://bookshop.europa.eu/uri?target=EUB:NOTICE:LD1A26347:EN:HTML oCLC: 948766866.
Geuzaine, C., Remacle, J.-F., 2009. Gmsh: a 3-D finite element mesh generator with built-in pre-and post-processing facilities. Int. J. Numer. Methods Eng. 79, 1309–1331.
Goniva, C., Kloss, C., Deen, N.G., Kuipers, J.A., Pirker, S., 2012. Influence of rolling friction on single spout fluidized bed simulation. Particuology 10, 582–591. https://doi.org/10.1016/j.partic.2012.05.002. URL. https://linkinghub.elsevier.com/retrieve/pii/S1674200112001356.
Hazen, A., 1892. Some physical properties of sand and gravels, with special reference to their use in filtration. In: 24th Annual Rep., Massachusetts State Board of Health, vol. 24, pp. 539–556. Pub. Doc. NA°34.
Hirsch, C., 2007. Numerical Computation of Internal and External Flows: Fundamentals of Computational Fluid Dynamics, second ed. Elsevier/Butterworth-Heinemann. OCLC, Oxford ; Burlington, MA. ocn148277909.
Issa, R., 1986. Solution of the implicitly discretised fluid flow equations by operator-splitting. J. Comput. Phys. 62, 40–65. https://doi.org/10.1016/0021-9991(86)90099-9. URL. https://linkinghub.elsevier.com/retrieve/pii/0021999186900999.
Kloss, C., Goniva, C., Hager, A., Amberger, S., Pirker, S., 2012. Models, algorithms and validation for opensource DEM and CFD-DEM. *Progress in computational fluid dynamics*. Int. J. 12, 140. https://doi.org/10.1504/PCFD.2012.047457. URL. http://www.inderscience.com/link.php?id=47457.
Kuang, S., Zhou, M., Yu, A., 2020. CFD-DEM modelling and simulation of pneumatic conveying: a review. Powder Technol. 365, 186–207. https://doi.org/10.1016/j.powtec.2019.02.011. URL. https://linkinghub.elsevier.com/retrieve/pii/S003259101930107X.
Kuruneru, S.T., Marechal, E., Deligant, M., Khelladi, S., Ravelet, F., Saha, S.C., Sauret, E., Gu, Y., 2019. A comparative study of mixed Resolved-Unresolved CFD-DEM and unresolved CFD-DEM methods for the solution of particle-laden liquid flows. Arch. Comput. Methods Eng. 26, 1239–1254. URL. http://link.springer.com/10.1007/s11831-018-9282-3. doi:10.1007/s11831-018-9282-3.
Lahiri, S., Ghanta, K., 2010. Slurry flow modelling by CFD. Chem. Ind. Chem. Eng. Q. 16, 295–308. https://doi.org/10.2298/CICEQ091030034L.
Lambe, T.W., Whitman, R.V., 1969. *Soil Mechanics*. Series in Soil Engineering. Wiley, New York.
Lyons, B., 2014. *Produced water: asset or waste?*. Atlantic Council of the United States. URL. http://www.atlanticcouncil.org/images/publications/Produced_Water_Asset_or_Waste.pdf oCLC: 907978973.
Mao, J., Zhao, L., Liu, X., Avital, E., 2020. A resolved CFDEM method for the interaction between the fluid and the discontinuous solids with large movement. Int. J. Numer. Methods Eng. 121, 1738–1761. URL. https://onlinelibrary.wiley.com/doi/abs/10.1002/nme.6285. doi:10.1002/nme.6285.
Mondal, S., Wu, C., Sharma, M.M., 2016. Coupled CFD-DEM simulation of hydrodynamic bridging at constrictions. Int. J. Multiphas. Flow 84, 245–263. https://doi.org/10.1016/j.ijmultiphaseflow.2016.05.001. URL. https://linkinghub.elsevier.com/retrieve/pii/S0301932216302580.
Muskat, M., Meres, M.W., 1936. The flow of heterogeneous fluids through porous media. Physics 7, 346–363. URL. http://aip.scitation.org/doi/10.1063/1.1745403. doi:10.1063/1.1745403.
Muskat, M., Wyckoff, R., Botset, H., Meres, M., 1937. Flow of gas-liquid mixtures through sands. Transactions of the AIME 123, 69–96. URL. http://www.onepetro.org/doi/10.2118/937069-G. doi:10.2118/937069-G.
Odong, J., 2007. Evaluation of empirical formulae for determination of hydraulic conductivity based on grain-size analysis. Journal of American Science 3, 54–60. URL. http://www.jofamericanscience.org/journals/am-sci/0401/01_0287_JustineOdong_Evaluation_am0401.pdf. doi:10.7537/marsjas040108.01.
Pozrikidis, C., 2011. Introduction to Theoretical and Computational Fluid Dynamics. Oxford University Press, New York.
Pöschel, T., Schwager, T., 2010. Computational Granular Dynamics: Models and Algorithms, first ed. Springer Berlin. OCLC, Berlin, p. 934513120.
Salarashayeri, A., Siosemarde, M., 2012. Prediction of soil hydraulic conductivity from particle-size distribution. World Academy of Science, Engineering and Technology 61, 454–458. URL. https://publications.waset.org/1747/prediction-of-soil-hydraulic-conductivity-from-particle-size-distribution.
Shor, R.J., Sharma, M.M., 2014. Reducing proppant flowback from fractures: factors affecting the maximum flowback rate. SPE Hydraulic Fracturing Technology Conference. Society of Petroleum Engineers, The Woodlands, Texas, USA. URL. http://www.onepetro.org/doi/10.2118/168649-MS. doi:10.2118/168649-MS.
Silbert, L.E., Ertaş, D., Grest, G.S., Halsey, T.C., Levine, D., Plimpton, S.J., 2001. Granular flow down an inclined plane: bagnold scaling and rheology. Phys. Rev. 64, 051302 https://doi.org/10.1103/PhysRevE.64.051302. URL. https://link.aps.org/doi/10.1103/PhysRevE.64.051302.
Versteeg, H.K., Malalasekera, W., 2011. An Introduction to Computational Fluid Dynamics: the Finite Volume Method. Prentice Hall, Harlow. OCLC: 751517337.
Wang, J., Elsworth, D., Denison, M.K., 2018. Propagation, proppant transport and the evolution of transport properties of hydraulic fractures. J. Fluid Mech. 855, 503–534. URL. https://www.cambridge.org/core/product/identifier/S0022112018006705/type/journal_article. doi:10.1017/jfm.2018.670.
Washino, K., Chan, E.L., Miyazaki, K., Tsuji, T., Tanaka, T., 2016. Time step criteria in DEM simulation of wet particles in viscosity dominant systems. Powder Technol. 302, 100–107. URL. https://linkinghub.elsevier.com/retrieve/pii/S0032591016305010. doi:10.1016/j.powtec.2016.08.018.
Zhang, H.P., Makse, H.A., 2005. Jamming transition in emulsions and granular materials. Phys. Rev. 72, 011301. URL. https://link.aps.org/doi/10.1103/PhysRevE.72.011301. doi:10.1103/PhysRevE.72.011301.
Zhu, H., Zhou, Z., Yang, R., Yu, A., 2007. Discrete particle simulation of particulate systems: theoretical developments. Chem. Eng. Sci. 62, 3378–3396. URL. https://linkinghub.elsevier.com/retrieve/pii/S000925090700262X. doi:10.1016/j.ces.2006.12.089.
Zuriguel, I., 2014. Invited review: Clogging of granular materials in bottlenecks. Pap. Phys. 6, 060014. URL. http://papersinphysics.org/index.php/papersinphysics/article/view/231. doi:10.4279/pip.060014.
Zuriguel, I., Parisi, D.R., Hidalgo, R.C., Lozano, C., Alvaro, J., Gago, P.A., Peralta, J.P., Ferrer, L.M., Pugnaloni, L.A., Clément, E., Maza, D., Pagonabarraga, I., Garcimartín, n A., 2015. Clogging transition of many-particle systems flowing through bottlenecks. Sci. Rep. 4, 7324. URL. http://www.nature.com/articles/srep07324. doi:10.1038/srep07324.